



## The Role of Intermetallic Particles in Localized Corrosion of an Aluminum Alloy Studied by SKPFM and Integrated AFM/SECM

A. Davoodi,<sup>a,\*</sup> J. Pan,<sup>a,\*\*,z</sup> C. Leygraf,<sup>a,\*\*</sup> and S. Norgren<sup>b</sup>

<sup>a</sup>Division of Corrosion Science, Department of Chemistry, Royal Institute of Technology, SE-100 44 Stockholm, Sweden

<sup>b</sup>Sapa Technology, SE-612 81 Finspång, Sweden

Aluminum alloy EN AW-3003 contains a certain amount of micrometer-sized constituent particles and a large number of nanometer-sized dispersoids. The practical nobility of intermetallic particles relative to an alloy matrix was evaluated ex situ by scanning Kelvin probe force microscopy (SKPFM), and localized corrosion initiation of the alloy exposed to chloride solutions was studied in situ by integrated atomic force microscopy (AFM) and scanning electrochemical microscopy (SECM). The SKPFM results show a higher Volta potential for the constituent particles than the matrix, and a larger difference for larger particles. In some cases, the boundary region between the large constituents and the matrix exhibits a minimum Volta potential. In contrast, a small Volta potential difference was measured for the particles less than 1  $\mu\text{m}$ . The SECM mapping of the alloy surface in the solution provided evidence of a cathodic action of some constituent particles and a local anodic dissolution adjacent to them. Concurrent AFM and SECM images indicate that only some of the constituents are prone to initiate localized corrosion. Moreover, in situ AFM observations confirm enhanced localized dissolution in the boundary regions, verifying the cathodic character of the constituent particles and a microgalvanic effect on localized corrosion. The fine dispersoids of nanometer size seem to have no effect on the corrosion initiation.

© 2008 The Electrochemical Society. [DOI: 10.1149/1.2883737] All rights reserved.

Manuscript submitted November 15, 2007; revised manuscript received January 10, 2008.  
Available electronically March 12, 2008.

The alloying elements and microstructure play a very important role in localized corrosion of aluminum alloys. On commercially pure aluminum, pitting corrosion in crystallographic form was reported to occur along closely packed planes.<sup>1-5</sup> By increasing the alloying elements, an increased amount of intermetallic particles (IMPs) may form, and pits become insensitive to crystallographic structure but are associated with the IMPs and also slightly localized along grain boundaries. Reports about pitting corrosion of aluminum alloys were reviewed by Frankel<sup>6</sup> and Szklarska-Smialowska.<sup>7</sup> The influence of IMPs on localized corrosion of aluminum alloys has been widely recognized, and to elucidate their role has been the target of scientific research for decades. Recently, a survey of electrochemical characteristics of IMPs in aluminum alloys was reported, showing that corrosion potentials and pitting potentials vary over a wide range for various types of IMPs.<sup>8</sup>

To understand the exact role of IMPs in localized corrosion of aluminum alloys, especially the initial stage, requires high-resolution techniques that are able to characterize the IMPs and to probe localized corrosion process related to them. High-resolution imaging and analytical techniques like scanning electron microscopy (SEM) and transmission electron microscopy (TEM) have long been used for the characterization of the IMPs, but they are ex situ techniques and must be performed in a vacuum condition, and the surface status may change during the transition from the solution to the vacuum chamber. Optical microscopy was used in situ to visualize the morphology change during aluminum pitting in chloride solutions,<sup>3,4</sup> but the resolution was limited by the visible light. In recent years, micro- and nanoscale resolution techniques have shown possibilities to evaluate the corrosion tendency related to the IMPs, both ex situ and in situ, and to monitor ongoing corrosion processes on the alloy surface. To overcome the limitation of visible light, near-field scanning optical microscopy<sup>9</sup> and later on, in situ confocal laser scanning microscopy<sup>10,11</sup> were used to study the localized corrosion and trench formation around IMPs.

Atomic force microscopy (AFM) is another high-resolution imaging technique, which can be used either in situ or ex situ to monitor surface topography changes during the localized corrosion of

aluminum alloys.<sup>12-14</sup> Recently various functional abilities have been added to AFM to obtain other surface properties, which can be related to the corrosion behavior. Scanning Kelvin probe force microscopy (SKPFM) has been developed in order to visualize both the topography and Volta potential variations on the local surface area. The Volta potential value has been shown to correlate with the corrosion potential, and can be regarded as a measure of practical nobility.<sup>15,16</sup> However, this technique cannot be used in situ in aqueous solutions, and caution is needed when interpreting the Volta potential data.<sup>17-19</sup> It was also reported that, in some cases, the sample preparation created artifacts, suggesting that its influence on the Volta potential data should be considered.<sup>20</sup>

In order to visualize local electrochemical activities on the surface, scanning electrochemical microscopy (SECM) was performed on aluminum alloys in corrosive media.<sup>21,22</sup> SECM measures differences in local chemistry of the solution close to the sample surface, which provides the variations in local activity on the surface. However, there is a demand to increase the lateral resolution of the SECM and also to precisely control the distance between the electrode and sample. Taking advantage of the high resolution of AFM, an integrated AFM and SECM technique has been developed, which is capable of simultaneously mapping the topography and electrochemical activity on the same surface in the solution during ongoing corrosion processes.<sup>23,24</sup>

It seems that none of the techniques alone can provide all the information needed to understand the role of IMPs in the localized corrosion of aluminum alloys. A combination of various in situ and ex situ local probing techniques is necessary to achieve the goal. In this work, the aim is to improve the understanding of the role of IMPs in localized corrosion initiation by combining several complementary techniques: ex situ analysis of the IMPs by SEM/EDS, evaluation of their practical nobility by SKPFM, in situ mapping of local cathodic activity and anodic dissolution related to the IMPs by the integrated AFM/SECM, as well as in situ AFM monitoring of the localized corrosion process. This paper focuses on the results from combined ex situ and in situ measurements using high-resolution characterization and probing techniques. A parallel paper reports more mechanistic aspects of localized corrosion of the aluminum alloy and the influence of the IMPs.<sup>25</sup>

\* Electrochemical Society Student Member.

\*\* Electrochemical Society Active Member.

<sup>z</sup> E-mail: jinshanp@kth.se

### Experimental

**Sample material and preparation.**—The sample material EN-AW 3003 (Al–Mn alloy) was taken from conventional production. The alloy was direct chill cast to produce an ingot of 360 mm thickness. The ingot was homogenized for several hours at 600°C, which improved the formability of the material. Prior to hot rolling, the ingot was preheated up to about 520–540°C to ease rolling down to 3.0 mm coil thickness. The coil was cold-rolled down to 0.35 mm for full hardness temper without any intermediate anneal. To simulate a brazing operation of heat transfer materials, an A4 size sheet was heated to 600°C within 24 min in a nitrogen atmosphere, followed by relatively slow cooling (<0.5°C/s) resulting in a fully soft-annealed temper. The chemical analysis of the alloy melt prior to casting showed the following composition: 1.1% Mn, 0.50% Fe, 0.13% Si, 0.11% Cu (in wt %). Small samples of 5 × 1 mm size were cut out from the sheet, and the studied sections were longitudinal to the rolling direction. The small samples were mounted to a sample holder of brass using conductive silver glue. It was pre-coated using a diluted porofix and embedded in a porofix mold from Struers.

For the SEM analysis of the microstructure, X-ray energy-dispersive (EDS) analysis of the IMPs, and the local electrochemical measurements, the sample surface was first ground in several steps down to 2400 grit using SiC grinding paper, with ethanol cleaning between all steps. Prior to the analysis and local electrochemical experiments, the sample was finally polished using a silica suspension of pH 10 (OP-S suspension from Struers), and subsequently cleaned in ethanol using a polishing cloth. Acetone cleaning was avoided because it was previously shown to introduce corrosion on the surface.<sup>26,27</sup>

For the SKPFM measurements, the samples were usually prepared following the normal grinding and polishing procedures mentioned above. Additionally, a mechanical sample preparation using an ultramicrotome was performed to check the influence of sample preparation. This technique has been recently applied for AFM sample preparation for advantages such as providing a highly smooth surface without contaminations.<sup>20,28</sup> In this work, the sample was first trimmed by using a Leica Cryotrim 45, and then cut using a Leica Ultracut UC6 with a diamond knife. Sectioning with oscillation was performed with a 25 nm section thickness and a slow sectioning speed of 0.6 mm/s. The oscillating step was used to avoid knife marks. Moreover, it helps to get less pullout of the IMPs from the alloy matrix, giving the best performance of the UC6 Ultramicrotome.

**SEM-EDS analysis of IMPs.**—A Philips XL30S FEG-SEM was used for microstructure characterization and elemental analysis of the intermetallic particles. Micrographs were taken both for the scattered electrons (SE mode), which gives topography, and for the backscattered electrons (BSE mode). In the BSE mode the elemental content can be better distinguished because the particles containing heavier elements than the metal matrix will appear brighter in the SEM micrographs. Moreover, the EDS analysis of the composition was made on the intermetallic particles. Selected large IMPs were analyzed individually, taking into account the contribution from the alloy matrix. The nanosize dispersoids were analyzed by using SEM/EDS and X-ray diffraction (XRD) at Sapa Technology according to the established etching method, i.e., dissolution of the sample in butanol.<sup>29</sup> The composition so obtained should be regarded as an approximation of the IMPs.

**SKPFM characterization of IMPs.**—To evaluate the relative nobility of the IMPs in the alloy, SKPFM measurements were performed to map Volta potential variations on the prepared sample surface. The principle and details of the SKPFM technique have been described previously.<sup>15,30</sup> Two AFM instruments were used for the measurements. One of them was a commercial AFM instrument (Thermomicroscope) available at the Swedish Corrosion and Metals Research Institute (KIMAB), and in this case the signals for both the

topography and Volta potential were acquired simultaneously. In this approach the tip was very close to the surface, whereby the highest possible resolution could be obtained. The disadvantage of this procedure is that the topography signal may have an influence on the Volta potential data, giving some artifacts. For this instrument, the tip was made of SiN and coated with Ag, and the relative humidity in the chamber was 40%.<sup>30</sup>

Another instrument used was a Nanoscope IV at the Nano-Fab Laboratory at the Royal Institute of Technology, with the facilities for Volta potential measurement. In this approach the data were acquired in a two-pass mode.<sup>15</sup> In the first pass, the topography data were collected with the feedback control. Then, the probe was lifted up to a certain distance for the second pass scan to collect Volta potential data at a constant distance from the surface (between 50 and 100 nm in this work, depending on the roughness of the surface). The benefit of this procedure is that the topography and Volta potential signals are independent of each other, and there is no artifact due to signal cross talking. However, it takes twice the time to collect the data for the topography and Volta potential as the one-pass mode. The probe was antimony-doped Si, supplied by Veeco, and the instrument was placed in a clean room laboratory (class ISO 3 according to standard ISO 14644–1). The measurement of the ultramicrotome cut sample was performed using this instrument.

**AFM-SECM measurement of local activity.**—To investigate the local electrochemical activity related to the IMPs, integrated AFM/SECM measurements were performed for the mechanically polished sample in diluted NaCl solutions at cathodic or anodic polarization, as well as at open-circuit potential (OCP). The instrument used was a Resolver from Quesant Ltd., equipped with the iProbe package supplied by Windsor Scientific Ltd., U.K. Details of the instrument have been described previously.<sup>23,24</sup> A homemade electrochemical cell 2 cm in diameter and 1.5 cm in height was used for the measurements. A saturated Ag/AgCl and Pt foil were used as the reference and counter electrodes, respectively. Reagent chemicals and distilled water were used to make up the solutions. The integrated AFM/SECM measurements were performed using a dual-mode probe and a redox mediator. The voltammogram of the ultramicroelectrode tip in the solution with the redox mediator was characterized to define its working potential range. During the AFM/SECM measurement, the sample was held at the OCP or polarized, and the ultramicroelectrode was controlled at a defined working potential for maximum collection of the local current. With a ca. 3 mm long bending part of the dual-mode probe, it was able to scan the surface in the solution while leaving the laser reflection part above the solution.

For mapping the cathodic activity on the sample surface, a cathodic polarization was applied to the sample. The cathodic reactions are reduction of the redox mediator and possibly also of dissolved oxygen occurring on the surface (acting as a catalyst). Local surface sites with a higher cathodic activity, e.g., cathodic IMPs, result in an enhanced reduction rate on such sites, diffusion of the reduced mediator toward the ultramicroelectrode tip, and subsequent oxidation of the reduced mediator at the tip. Under anodic polarization, the SECM was operating in sample-generator-tip-collector mode, during which local surface areas of higher anodic activity ( $\text{Al} \rightarrow \text{Al}^{3+} + 3\text{e}^-$ ) cause a reduction of the redox mediator on these areas, diffusion of the reduced mediator toward the tip, and subsequent oxidation of the mediator at the tip. By scanning over the surface, concurrent AFM topography and SECM current maps of the same area were obtained. The lateral resolution of the SECM depends on the tip size, the sample-tip distance, and the electrolyte conductivity.<sup>31,32</sup> In an effort to map the anodic and cathodic active sites on the alloy surface under OCP conditions, the SECM mapping was performed after the anodic polarization of the sample was terminated, while the microelectrode was kept at the same working potential.

Due to the compromise of the dual-mode probe design, the quality of the AFM images from the integrated AFM/SECM usually is

not as good as what can be achieved by a standard AFM. Therefore, some complementary in situ AFM measurements were performed using a standard SiN cantilever, before or after the integrated AFM/SECM measurement, to achieve a better quality of the AFM topography image.

### Results and Discussion

**General microstructure characterization.**—The SEM/EDS and XRD analysis were reported in a parallel paper.<sup>25</sup> The results shows that, in the EN AW-3003 alloy, generally there are two distinct types of eutectically formed constituent IMPs (ca. 0.5 up to 10  $\mu\text{m}$  in size): the  $\alpha\text{-Al}(\text{Mn,Fe})\text{Si}$  phase, typically  $\text{Al}_{15}(\text{Mn,Fe})_3\text{Si}_2$ , and the  $\text{Al}(\text{Mn,Fe})$  phase, typically  $\text{Al}_6(\text{Mn,Fe})$ , which appear lighter in the BSE-SEM images. The difference between the two IMP types lies in the Si content and a different ratio of Al to (Mn,Fe). The ratio between Mn and Fe in these large constituent IMPs varies but is typically about 1:1. Changing the Mn and Fe content of the bulk composition will alter this ratio. The phases of the IMPs were identified in early studies at Sapa Technology as mentioned in the Experimental section.

Depending on the heat treatment, it is also possible to form finer IMPs of 0.1–0.5  $\mu\text{m}$  in size by a solid-state reaction in the Al–Mn alloys. Such particles are usually called dispersoids and contain mainly Al and Mn, e.g., AlMn dispersoids. Cu may also be incorporated, especially when the Cu content increases. Because Fe solubility is low in the solid Al matrix, Fe forms constituent eutectic particles during the solidification; hence, there is only a trace amount of Fe in such dispersoids. If the Si content in the material is above 0.10 wt % these dispersoids will contain some Si, also known as  $\alpha\text{-AlMnSi}$ -type dispersoids, typically as  $\alpha\text{-Al}_{12}\text{Mn}_3\text{Si}_{1-2}$ . The EN-AW 3003 alloy studied, with 0.13 wt % Si, may contain both types of dispersoids. During further heat-treatment, such as a brazing operation, the dispersoids may dissolve or reprecipitate, probably as very fine precipitates less than  $<0.1 \mu\text{m}$  size in grain boundaries.

In short, the composition of the IMPs may vary with size. The large constituent IMPs (micrometer size) contain Fe, whereas fine dispersoids (nm size) usually do not contain Fe. For the constituent IMPs, the  $\text{Al}(\text{Mn,Fe})\text{Si}$  type contains Si, whereas the  $\text{Al}(\text{Mn,Fe})$  type does not contain Si, and the ratio between Mn and Fe may vary to a certain extent. For the dispersoids, one type contains mainly Al and Mn, and another type also contains Si, with a varying Si content. Moreover, a large particle may have a heterogeneous composition within the particle. Figure 1 shows a BSE-SEM micrograph of the polished sample surface, with both eutectic intermetallic constituents (larger particles) and solid-state precipitated fine dispersoid particles. In Fig. 1, examples of the EDS spectra are also given, showing a relatively high Fe content in the constituent particle and relatively high Si content of the dispersoids, respectively.

**SKPFM characterization of corrosion tendency of IMPs.**—After the SEM-EDS analysis, SKPFM mapping of the Volta potential was performed on the sample to evaluate the relative nobility (corrosion tendency) of the IMPs. As an example, Fig. 2 shows SKPFM and BSE-SEM images for two large elongated IMPs and a few smaller ones. Here, the sample surface was prepared by normal polishing procedures and the SKPFM image was obtained using the thermomicroscope instrument. It is clear that the IMPs have a higher Volta potential (brighter in the SKPFM image) compared to the matrix, which is an indication of the cathodic character of the IMPs in the localized corrosion process. The SKPFM data are influenced by the composition and thickness of the oxide film covering the surface, and adsorbed species at the surface. As discussed in the literature, the correlation between the Volta potential data obtained in air and the corrosion potential in solution is not straight forward, and caution is needed when interpreting the Volta potential data.<sup>15,17-19</sup>

In some cases, the boundary region between the matrix and constituent IMP exhibits a minimum of the Volta potential. As an example, Fig. 3 displays an SKPFM image and line profiles showing

the variations in the Volta potential from the matrix through the boundary to the IMPs. The image was obtained from the polished surface using the Thermomicroscope AFM instrument. In this case, there might be a slight influence of the topography on the Volta potential because of a possibility of signal cross talking during the one-pass operation of the instrument. Unfortunately, this is an inherent character of this type of instrument and cannot be avoided completely. Moreover, the polishing procedure may also induce some artifacts, because it may cause a slight etching of the boundary region. It was reported that a normal polishing process causes some selective dissolution and has an influence on the Volta potential value, and should be considered in quantitative evaluations of data.<sup>19</sup> Caution must be taken in the quantitative evaluation of the Volta potential data.

To check the influence of the polishing procedure on the Volta potential data, the SKPFM measurements were performed on the sample prepared by the Ultramicrotome cutting, which is able to create a very flat surface without contamination. In this case, the Nanoscope IV instrument was used, with the two-pass mode, so there was no considerable risk for signal cross talking. Figure 4 shows the Volta potential variations across the matrix and large IMPs. The IMPs can hardly be seen in the AFM image of the flat surface (the height variation was less than 50 nm), but exhibit clearly higher Volta potential than the matrix. The difference in the Volta potential (ca. 700 mV for the large IMP) is almost the same as that obtained using the thermomicroscope instrument. Furthermore, a Volta potential minimum was also observed in the boundary region, appearing like a darker ring surrounding the large IMP. In this case, the Volta potential drop (ca. 100 mV) is less than that observed on a normally polished surface. One can see a gradual increase in the Volta potential when moving from the boundary region to the core of the IMP. By careful examination of the images, it appears that there are much less fine dispersoids in the boundary region (2–3  $\mu\text{m}$  width). One should be aware that the ultramicrotome cutting might also have an influence on the absolute value of the Volta potential, due to uneven compression stresses created in the areas of harder IMPs and softer matrix. Nevertheless, the results verify the observations about the cathodic character of the IMPs and also the minimum Volta potential in the boundary region adjacent to large IMPs. Importantly, the results indicate that the difference in the Volta potential between the IMP and the matrix is not considerably influenced by the polishing procedure used in this study.

The maximum Volta potential difference between the IMPs and matrix measured for EN AW-3003 in this work is significantly greater than that reported for the AA2024 alloy (up to 400–500 mV between  $\text{Al}_2\text{CuMg}$  particles and the matrix has been reported). The reason for this may be related to the difference in chemical composition between the IMPs and the matrix in the investigated alloy. From thermodynamic nobility considerations, in EN AW-3003, all the alloying elements (Mn, Fe, and Si) in the IMPs may lead to an increased Volta potential of the IMPs, resulting in a large difference in the Volta potential relative to the matrix. In AA2024, however, the cathodic type  $\text{Al}_2\text{CuMg}$  particles contain both Cu and Mg; the Cu content may lead to an increased Volta potential but the Mg content may have the opposite effect. As a result, the Volta potential difference between  $\text{Al}_2\text{CuMg}$  particles and the matrix is relatively smaller. Naturally the solubility of the alloying elements (Mn, Cu, Mg, Fe, and Si) in the alloy matrix also has an influence on the Volta potential of the alloy matrix.

Regarding the Volta potential gradient in the boundary region, it was reported that in AA2024 alloy shell-shaped particles precipitate after a long quench delay time.<sup>33</sup> A Volta potential minimum was observed between the shell-shaped particle and the matrix, indicating a highly localized galvanic coupling. The Volta potential minimum was interpreted as being associated with the shell of the particle, which seems to be a mistake, because the Volta potential image revealed that the shell exhibits the maximum Volta potential, whereas the minimum Volta potential appears to be associated with the boundary region adjacent to the shell-shaped particle. In this

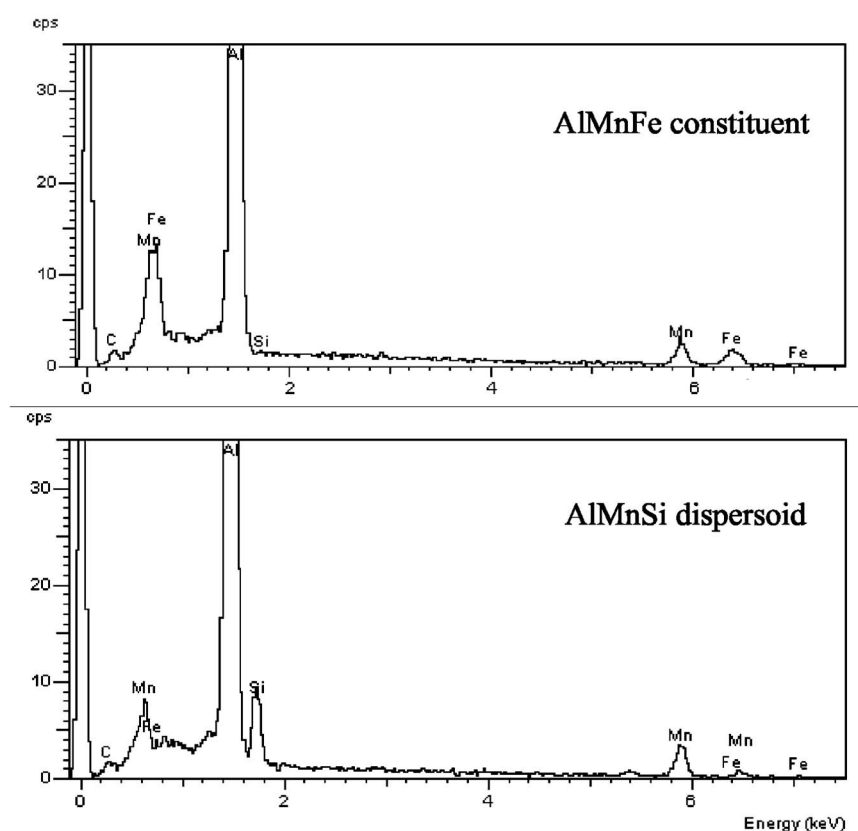
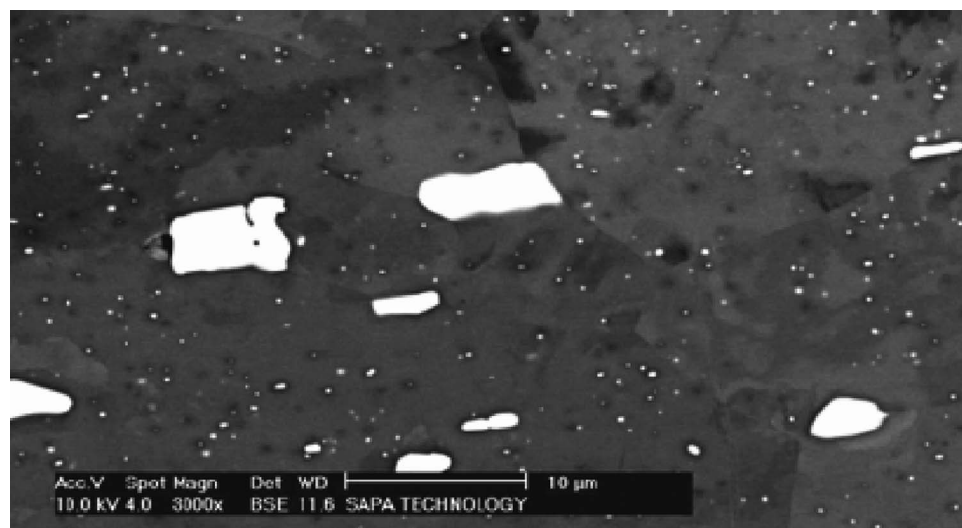


**Figure 1.** BSE-SEM micrograph of rolled EN AW-3003 alloy after braze-simulation treatment, with both eutectic intermetallic constituents (larger particles) and solid-state precipitated fine dispersoid particles, and examples of EDS analysis of the particles.

work on EN AW-3003 alloy, clearly the lowest Volta potential was observed in the boundary region around the large IMPs. The reason for this minimum Volta potential in the boundary region is probably related to the elemental diffusion during the formation of the IMPs rich in Mn, which results in Mn depletion and much less fine dispersoids in the boundary region. Moreover, the minimum Volta potential was sometimes observed in the boundary regions adjacent to elongated IMPs. This suggests that the mechanical deformation during the rolling which creates defects, e.g., voids, in the vicinity of the IMPs, also has an influence on the Volta potential. To clarify the detailed composition gradient across the boundary regions, further studies are necessary, using high-resolution analytical techniques such as TEM<sup>34</sup> and microscopic Auger electron spectroscopy.<sup>35</sup>

In this study, the SKPFM measurements of different IMPs revealed that the Volta potential may also vary with the IMPs size. A

high-resolution scan was performed for the nanometer-sized IMPs. In general, the SKPFM images show different Volta potential variations for large and small IMPs. For quantitative evaluation of the relative nobility of the IMPs, the Volta potential difference  $\Delta E$  was defined as the difference between the average highest potential of the IMP and the average of the matrix, as exemplified in Fig. 5, with a line profile showing the  $\Delta E$  for large, medium, and small IMPs, respectively. Unlike the absolute value of the Volta potential, the Volta potential difference,  $\Delta E$ , is not easily influenced by the measuring conditions as evidenced by the above results. This parameter may be regarded as a measure of the driving force for microgalvanic action in the localized corrosion. For a quantitative evaluation of the size dependence, the particle size was taken as the diameter for round-shaped IMPs and as the maximum length for elongated ones.

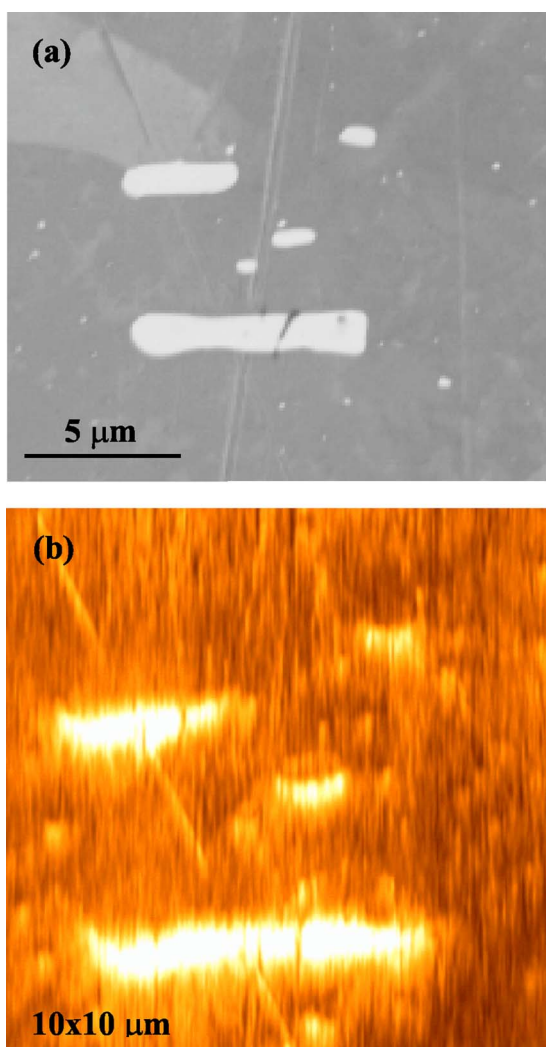


**Figure 2.** (Color online) (a) High-resolution SEM micrograph of polished surface of EN AW-3003 alloy, and (b) Volta potential map obtained by one-pass mode, on the same area, showing higher Volta potential of the IMPs. Volta potential Z scale 1 V.

The average Volta potential value was calculated using the software for data analysis. A baseline of zero value was chosen for the matrix. The data are plotted in Fig. 6 showing the relationship between the  $\Delta E$  and the size of the IMPs. In the figure, each data point represents one IMP, and the error bar indicates 5% deviation of the value because the Volta potential may also vary slightly on the surface of the same IMP. A general trend is that the  $\Delta E$  increases with the size of the IMP (but not linearly), and clearly the micrometer-sized constituent particles exhibit larger  $\Delta E$  than the nanometer-sized dispersoids. For the rare large IMPs 5–10  $\mu\text{m}$  in size the  $\Delta E$  may reach 0.8–1.0 V. In contrast, below ca. 0.5  $\mu\text{m}$ , the  $\Delta E$  is less than 200 mV, as shown in the inset diagram in Fig. 6. This is an interesting result from an application point of view. Because the corrosion initiation was mostly observed to occur adjacent to large IMPs (in situ AFM measurements<sup>14</sup>), it seem that these IMPs with  $\Delta E$  less than ca. 200 mV are not dangerous with respect to the localized corrosion. This implies that the fine dispersoids are not prone to initiating local dissolution of the aluminum alloy.

The size dependence of the Volta potential difference could be related to the composition of the IMPs. The fine dispersoids have different composition than the large constituent particles because of different formation processes during casting and hot rolling.<sup>25</sup> The larger ones are formed during the casting process through a eutectic

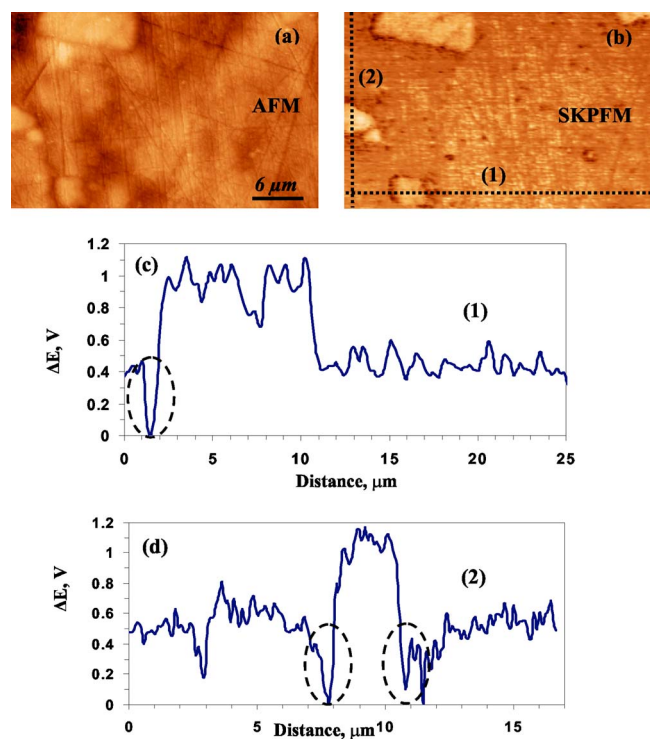


**Figure 3.** (Color online) (a) Topography and (b) Volta potential images of polished surface of EN AW-3003 alloy obtained by one-pass mode. (c), (d) Two Volta potential line profiles across the boundary between the IMPs and the matrix.

reaction at the end of the solidification for the ternary or quaternary systems of Al–Mn–Fe and the Al–Mn–Fe–Si.<sup>29,36–39</sup> This results in the Fe-rich particles since Fe has a low solubility (0.04 wt %) in

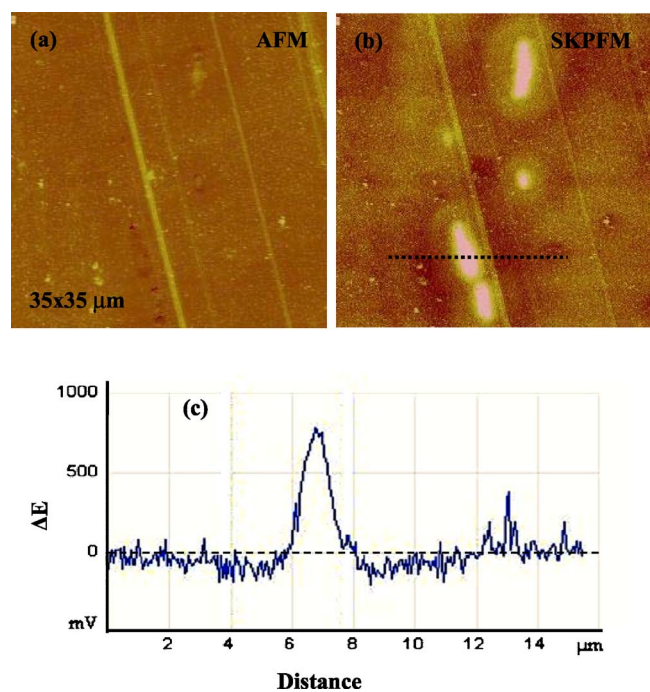


**Figure 4.** (Color online) (a) Topography and (b) Volta potential images of EN AW-3003 alloy obtained by two-pass mode, and (c) Volta potential line profile. The surface was prepared by ultramicrotome cutting. Height variation in topography image was 50 nm.

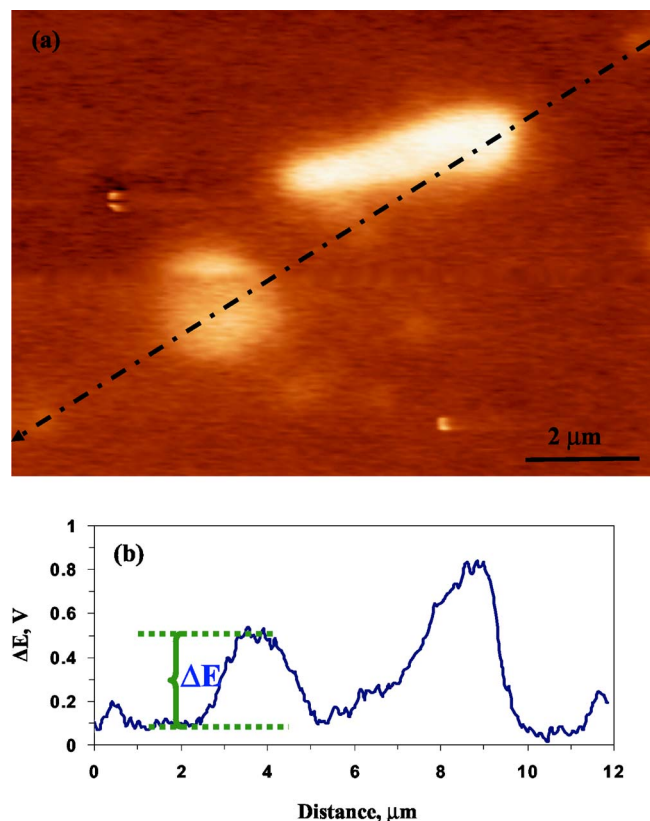


**Figure 5.** (Color online) (a) Volta potential image and (b) line profile showing the different levels of Volta potential between IMPs, dispersoids, and alloy matrix on a polished surface of EN AW-3003 alloy, obtained by a one-pass mode.

the primary  $\alpha$ -Al phase, whereas the solid solubility of Mn is approximately 1.8 wt % at the eutectic temperature. During the homogenization and preheating processes, Al–Mn (Al–Mn–Si) particles form through solid-state processes when the alloy cools down, resulting in the dispersoids of 0.5–2  $\mu\text{m}$ , which survive the brazing cycle. These consist mainly of the  $\alpha$ -AlMnSi phase and do not contain Fe.<sup>37</sup> Thus, the reason for different Volta potential of the IMPs is probably related to the difference in Fe and Si content of the different types of IMPs. The large data scattering for the IMPs of similar size (several micrometers) may be due to the variation in their Si content and Mn/Fe ratio. For the fine dispersoids

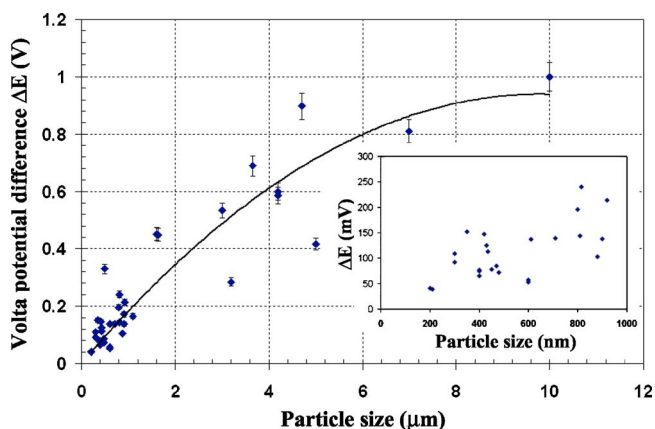


**Figure 6.** (Color online) Volta potential difference vs the IMPs size for EN AW-3003 alloy; the inset graph shows data for the IMPs smaller than 1  $\mu\text{m}$ .

(<0.5  $\mu\text{m}$ ) of AlMn or AlMnSi, the Cu content may also have an influence on the Volta potential. It was reported that in diluted NaCl solution an AlMn phase has a higher corrosion potential and pitting potential than an AlMnSi phase.<sup>8</sup> However, no such information could be found in the literature for the different types of IMPs investigated in this study.

For the finer dispersoids (<200 nm), a negligible Volta potential difference was detected in the measurements. This is probably because the Volta potential may have a contribution from the surrounding area that may dominate when measuring very small sites, so that only a negligible Volta potential difference can be detected for the smallest dispersoids in the matrix. It is known that the electric field sensed by the SKPFM tip is larger than the size of the tip itself.<sup>40</sup> This may also have an influence on the ability to resolve small particles in the Volta potential mapping, although the AFM tips used in this work are expected to give a good resolution in the potential mapping. This relation between size and Volta potential difference is only valid for this particular alloy type and composition.

Very recently, a statistical study combining AFM, SKPFM, and EDS analysis was carried out on Al<sub>2</sub>CuMg particles in AA2024 alloy to determine their corrosion behavior in chloride-containing solutions. The combination of these three techniques allowed the correlation of the dissolution depth of the particles to their Volta potential and chemical composition.<sup>41</sup> However, all the analyses were performed ex situ, and therefore there was no information about the corrosion behavior from individual particles. Below, we report the results from the in situ study by using the integrated AFM/SECM.

*Integrated AFM/SECM mapping of local cathodic and anodic activities.*— Integrated AFM/SECM measurements were performed for the sample in diluted NaCl solutions to visualize the cathodic activity of the IMPs and the anodic dissolution adjacent to them, and selected results were reported in the parallel paper.<sup>25</sup> The results from the measurements at cathodic polarization provide a direct evidence of enhanced cathodic activities on the surface of large IMPs, but not all of the large IMPs exhibit an enhanced cathodic activity. This can be explained by the different compositions of the large IMPs. The measurements at anodic polarizations reveal an enhanced anodic current due to the localized dissolution adjacent to some large IMPs, and also the dynamic nature of the local dissolution process.<sup>25</sup>

Figure 7 shows a high-resolution SECM image obtained in 20 mM NaCl solution with 5 mM KI as the redox mediator, at an anodic polarization of 200 mV. The elliptical shape of the enhanced anodic current most likely indicates the localized dissolution around an elongated IMP. In this case, the elongated IMP is large enough so that the local current around the IMP could be resolved by the SECM measurement, as shown by numerical simulation on the SECM operation.<sup>31,32</sup> The SECM image in Fig. 7 can be compared to an in situ AFM image in Fig. 8, which was obtained (not on the same area) after 6 h exposure in the solution. The observation provides support for localized corrosion occurring in the boundary region adjacent to large IMP, especially in the rolling direction.<sup>14</sup>

For the smaller IMPs or clusters of smaller IMPs, the enhanced current around the IMPs may appear only as a broad maximum, because the size of the IMP or the distance between the IMPs is too small for the current distribution to be laterally resolved by the SECM.<sup>31,32</sup> As an example, Fig. 9 displays concurrent topography AFM and SECM current images obtained under the same conditions as for Fig. 7, but on another surface area. The resolution of the AFM topography image in Fig. 9a was sacrificed in order to improve the resolution for the current mapping; no IMP particles can be clearly seen from the topography. However, the concurrent SECM image in Fig. 9b shows several micrometer-sized areas with enhanced anodic current probably originating from relatively small IMPs and/or clusters of the small IMPs. The limit of distance between the small active sites that can be resolved by the SECM was considered in the simulation of the integrated AFM/SECM probe, which indicates that

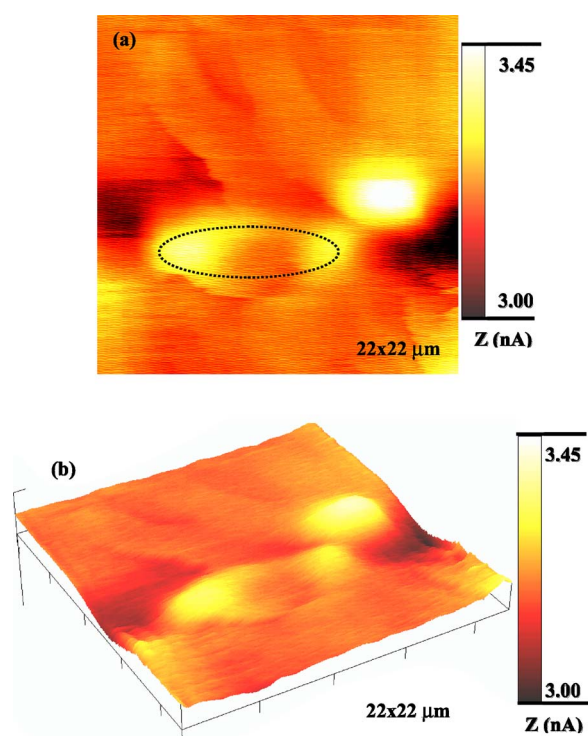


**Figure 7.** (Color online) (a) 2D and (b) 3D SECM images of the surface of the EN W-3003 alloy in 20 mM NaCl and 5 mM KI electrolyte at anodic polarization of 200 mV. The dotted ellipse highlights enhanced current on the boundary around an elongated IMP.

for small active sites of 1  $\mu\text{m}$  size the distance needs to be larger than 3–4  $\mu\text{m}$  in order to be resolved by the SECM.<sup>31,32</sup>

In this work, efforts were also made to map the anodic and cathodic activities of the alloy surface in the diluted NaCl solution at OCP conditions using the integrated AFM/SECM. At the open-circuit condition, the cathodic reaction (reduction of dissolved oxygen) occurring on the IMPs is coupled to the anodic reaction, i.e., corrosion of aluminum at active sites (e.g., IMP-matrix boundary or pits). Apparently, the kinetic of these reactions in the diluted NaCl solution at the OCP was not fast enough for the SECM to map the local electrochemical currents. Therefore, the SECM imaging was performed after the anodic polarization of 200 mV was terminated.

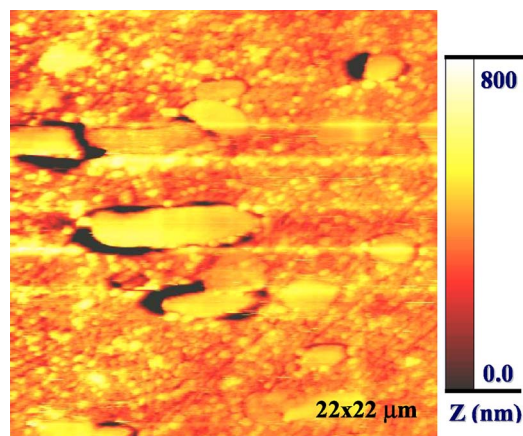


**Figure 8.** (Color online) In situ AFM image of the surface of the EN AW-3003 alloy after 6 h immersion in 20 mM NaCl and 5 mM KI solution, showing local dissolution in the boundary region around large constituent particles.

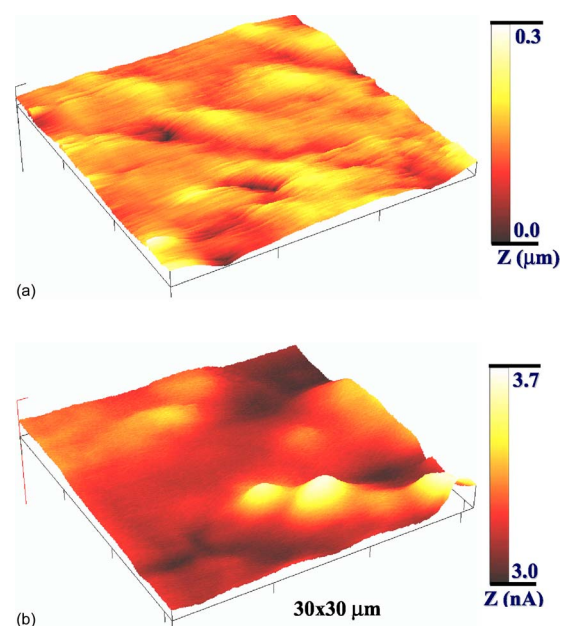


**Figure 9.** (Color online) (a) Concurrent AFM topography and (b) SECM current images of the surface of the EN AW-3003 alloy in 20 mM NaCl and 5 mM KI solution at anodic polarization of 200 mV.

In this case, local active dissolution already occurred on the alloy surface, as shown in Fig. 9, but the sample was at the OCP condition without any polarization. In this way, it was observed that the remaining anodic activities spread over the matrix surface, while the IMPs were likely acting as sites for cathodic reactions. The measurements reveal sites with much lower current than the surrounding area or even a negative current, and these sites remain at the same locations in repeated measurements. Judging from their size, these sites are likely the locations of the large IMPs exhibiting a cathodic property relative to the matrix. Due to substantial aluminum dissolution during the early anodic polarization, the solution chemistry became complicated and the cyclic voltammetry response of the microelectrode might have changed; thus, no effort was made to interpret the absolute value of the current. As an example, Fig. 10 shows an SECM image obtained, with a relative scale of current. These observations suggest a simultaneous anodic reaction on the alloy matrix and a cathodic reduction on the IMPs at the OCP con-

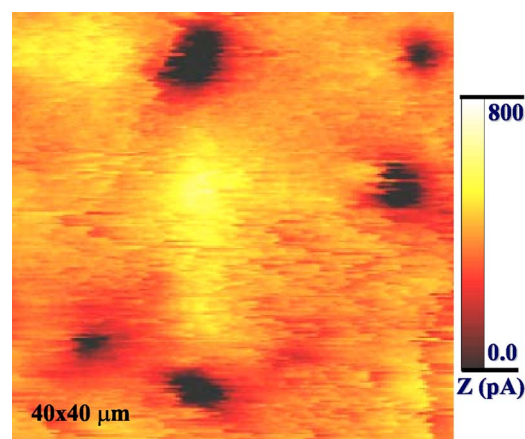


**Figure 10.** (Color online) SECM image of the surface of the EN W-3003 alloy in 20 mM NaCl and 5 mM KI solution at OCP conditions, after several minutes of anodic polarization of 200 mV.

dition. Further efforts are being made to obtain better concurrent AFM and SECM images at OCP under more controlled experimental conditions.

It has been reported that localized corrosion can occur on aluminum alloys due to their heterogeneous structure and the existence of IMPs and also of inclusions.<sup>10,13,14</sup> Statistical evaluations of location of localized attack on aluminum alloys have been performed and reveal the influence of constituent IMPs' composition, size, and clustering on the corrosion initiation.<sup>41,42</sup> In this work, the SKPFM mapping of the Volta potential clearly shows the cathodic character of the constituent IMPs relative to the alloy matrix, and a size dependence of the practical nobility of the constituent IMPs, which can be explained by the variations in their composition. The results from the integrated AFM/SECM measurements of local cathodic and anodic activities related to the IMPs demonstrate the cathodic action of the constituent IMPs and localized corrosion initiation induced by the IMPs. The observations confirm the microgalvanic effect of the constituent IMPs, and that the boundary region adjacent to some constituent IMPs, where a Volta potential minimum was detected, is indeed the preferential site for localized corrosion initiation. Similar observations were previously reported for the ferritic–austenitic phase boundary, where localized corrosion initiation was observed to occur.<sup>43</sup>

### Conclusion

AFM-based techniques, SKPFM and integrated AFM/SECM, have been used to evaluate the practical nobility of intermetallic particles in EN AW-3003 alloy, and to map the cathodic and anodic activities related to the particles involved in localized corrosion initiation in diluted NaCl solutions.

The Volta potential mapping reveals the cathodic character of the particles relative to the alloy matrix. The Volta potential difference between the particle and the matrix is large for eutectically formed, micrometer-sized constituent particles, but small for solid-state formed, nanometer-sized dispersoids, and negligible for fine dispersoids less than ca. 200 nm in size. The size dependence of the Volta potential difference can be explained by the variations in the content of Fe and Si of the particles. In some cases, the boundary region between large constituent particles and the matrix exhibits a minimum in the Volta potential.

The electrochemical activity mapping of the sample surface in diluted NaCl solutions shows direct evidence of the cathodic activity of the constituent particles, and localized anodic dissolution preferably occurring in the boundary region adjacent to large constituent particles. The results demonstrate a microgalvanic effect of the constituent particles in localized corrosion initiation, and confirm that the large constituent particles are more prone to initiate localized corrosion than small dispersoids, and the boundary region adjacent to large constituent particles is a weak point for local dissolution.

### Acknowledgments

Sapa Heat Transfer AB in Finspång, the Brinell Centre at Royal Institute of Technology in Stockholm, Sweden, and The Ministry of Science of Iran are acknowledged for the financial support. Dr. Rolf Gubner and Namurata Sathirachinda at KIMAB are acknowledged for the help with SKPFM measurements using the Veeco AFM in-

strument. Jan de Weert from Leica Microsystems AB is acknowledged for the help with ultramicrotome sample preparation.

Royal Institute for Technology assisted in meeting the publication costs of this article.

### References

1. R. C. Newman, *Corros. Sci.*, **37**, 527 (1995).
2. V. S. Sinyavskii, *Prot. Met.*, **73**, 469 (2001).
3. M. Baumgärtner and H. Kaesche, *Corros. Sci.*, **29**, 363 (1989).
4. M. Baumgärtner and H. Kaesche, *Corros. Sci.*, **31**, 231 (1990).
5. R. Ambat, A. J. Davenport, G. M. Scamans, and A. Afseth, *Corros. Sci.*, **48**, 3455 (2006).
6. G. S. Frankel, *J. Electrochem. Soc.*, **145**, 2186 (1998).
7. Z. Szklarska-Smialowska, *Corros. Sci.*, **41**, 1743 (1999).
8. N. Birbilis and R. G. Buchheit, *J. Electrochem. Soc.*, **152**, B140 (2005).
9. M. Büchler, J. Kerimo, F. Guillaum, and W. H. Smyrl, *J. Electrochem. Soc.*, **147**, 3691 (2000).
10. G. O. Ilevbare, O. Schneider, R. G. Kelly, and J. R. Scully, *J. Electrochem. Soc.*, **151**, B453 (2004).
11. O. Schneider, G. O. Ilevbare, J. R. Scully, and R. G. Kelly, *J. Electrochem. Soc.*, **151**, B465 (2004).
12. P. Schmutz and G. S. Frankel, *J. Electrochem. Soc.*, **146**, 4461 (1999).
13. J. O. Park, C. H. Paik, Y. H. Huang, and R. C. Alkire, *J. Electrochem. Soc.*, **146**, 517 (1999).
14. A. Davoodi, J. Pan, C. Leygraf, and S. Norgren, *Appl. Surf. Sci.*, **252**, 5499 (2006).
15. V. Guillaumin, P. Schmutz, and G. S. Frankel, *J. Electrochem. Soc.*, **148**, B163 (2001).
16. M. Rohwerder, E. Hornung, and M. Stratmann, *Electrochim. Acta*, **48**, 1235 (2003).
17. F. Andreatta, H. Terryn, and J. H. W. de Wit, *Electrochim. Acta*, **49**, 2851 (2004).
18. J. H. W. de Wit, *Electrochim. Acta*, **49**, 2841 (2004).
19. T. H. Muster and A. E. Hughes, *J. Electrochem. Soc.*, **153**, B474 (2006).
20. B. S. Tanem, G. Svenningsen, and J. Mårdalen, *Corros. Sci.*, **47**, 1506 (2005).
21. I. Serebrennikova and H. S. White, *Electrochem. Solid-State Lett.*, **4**, B4 (2001).
22. J. C. Seegmiller and D. A. Buttry, *J. Electrochem. Soc.*, **150**, B413 (2003).
23. A. Davoodi, J. Pan, C. Leygraf, and S. Norgren, *Electrochem. Solid-State Lett.*, **8**, B21 (2005).
24. A. Davoodi, J. Pan, C. Leygraf, and S. Norgren, *Electrochim. Acta*, **52**, 7697 (2007).
25. A. Davoodi, J. Pan, C. Leygraf, and S. Norgren, *J. Electrochem. Soc.*, **155**, C138 (2008).
26. D. Chidambaram and G. P. Halada, *Surf. Interface Anal.*, **31**, 1056 (2001).
27. S. V. Kagwade, C. R. Clayton, D. Chidambaram, M. L. Du, and F. P. Chiang, *J. Electrochem. Soc.*, **147**, 4125 (2000).
28. F. Echeverria, P. Skeldon, G. E. Thompson, J. R. Walton, H. Habazaki, and K. Shimizu, *Electrochem. Solid-State Lett.*, **1**, 24 (1998).
29. C. J. Simensen, P. Fartum, and A. Andersen, *Fresenius' Z. Anal. Chem.* **319**, 286 (1984).
30. M. Jönsson, D. Thierry, and N. LeBozec, *Corros. Sci.*, **48**, 1193 (2006).
31. A. Davoodi, A. Farzadi, J. Pan, and C. Leygraf, *J. Electrochem. Soc.*, Submitted.
32. A. Davoodi, A. Farzadi, J. Pan, and C. Leygraf, *J. Electrochem. Soc.*, Submitted.
33. P. Campestrini, E. P. M. van Westing, H. W. van Rooijen, and J. H. W. de Wit, *Corros. Sci.*, **42**, 1853 (2000).
34. Q. Meng and G. S. Frankel, *J. Electrochem. Soc.*, **151**, B271 (2004).
35. M. Femenia, J. Pan, and C. Leygraf, *J. Electrochem. Soc.*, **151**, B581 (2004).
36. J. E. Tibballs, J. A. Horst, and C. J. Simensen, *J. Math. Sci.*, **36**, 937 (2001).
37. A. Bahadur, *J. Math. Sci.*, **23**, 48 (1988).
38. V. Raghavan, *J. Phase Equilib.*, **28**, 192 (2007).
39. V. Raghavan, *J. Phase Equilib.*, **28**, 215 (2007).
40. H. O. Jacobs, P. Leuchtman, O. J. Homan, and A. Stemmer, *J. Appl. Phys.*, **84**, 1168 (1998).
41. L. Lacroix, L. Ressler, C. Blanc, and G. Mankowski, *J. Electrochem. Soc.*, **155**, C8 (2008).
42. D. G. Harlow, M. Z. Wang, and R. P. Wei, *Metall. Mater. Trans. A*, **37**, 3367 (2006).
43. M. Femenia, Ph.D. Thesis, Royal Institute of Technology, Stockholm (2003).